1

Interaction of the Nuclear Radiation with Detector Absorbers

Introduction

Radiation sensors are intended for the qualitative detection of various elementary nuclear particles and, in many applications, measure their quantitative characteristic parameters, such as flux, energy distribution, position coordinates, timing information, etc. The detection starts from a moment when an incoming particle interacts with the sensor's active volume. In some publications on the radiation measurements, the authors proceed directly to the down-conversion process transforming deposited nuclear particle energy E_p into either a corresponding number of quasiparticles N_{qp} in *nonthermal* devices or a temperature rise ΔT in *thermal calorimeters* in proportion to E_p. If that was true, detectors exposed to the monochromatic beam would be producing a single peak output on the energy spectrum centered at E_p. In practice, however, we normally observe spectra enriched by excitations of secondary characteristic radiations, background events, escape or double peaks, tales, etc. This enrichment is further superimposed by the incomplete charge collection due to various transport loss mechanisms and sensor/readout noise. Very often, we have to apply quite complex mathematical models solving inverse problems to restore energy and timing information of incoming nuclear particles. To do that efficiently, it is useful to divide the detection process into four phases:

1) The primary nuclear reaction of a particle with the absorber matter, which will be the topic of the present chapter.
2) The energy down-conversion process generating a response in proportion to the energy deposited in the active volume.
3) The drift/diffusion of generated informative carriers toward the sensor collection electrodes.
4) The measurement process of a signal generated by a radiation absorber with one of the sensor types, e.g. the tunnel junction, transition edge thermometer, kinetic inductance, semiconductor barrier, etc.

The down-conversion and transport in superconducting, semiconducting, and normal metal absorbers will be discussed in the corresponding sections of Chapters 2, 3, and 4.

The quantum cryogenic sensors presented in this manuscript are capable to respond to practically all types of known radiations: charged particles, optical photons from infrared to X-rays and γ-rays, and uncharged particles, e.g. neutrons and weakly interacting massive particles (WIMPs). Among these types, only electrons are capable to initiate and participate *directly* in the energy down-conversion process through the inelastic electron–electron and electron–phonon interactions. Detection techniques of other particles involve *indirect* energy cascades. In the indirect cascades, the primary interactions liberate normally energetic atomic electrons (δ-ray), which further act as light charge particles creating on their path a measurable amount of quasiparticles in a chain of secondary processes: ionization (semiconductors), or the Cooper electron pair-breaking (superconductors), or hot-electron carrier generation (normal metal absorbers).

There are two basic energy exchange reaction mechanisms between the primary nuclear particles and target atoms: the *absorption* and the *inelastic scattering*. The inelastic scattering events take place when incoming particles share their kinetic energy with atomic and free electrons by electromagnetic interactions.

Figure 1.1.1 illustrates schematically the absorption process, in which an incident particle disappears completely captured by the target matter. These interactions are more typical for the photon beams, although charged particles can equally be absorbed in nuclear reactions to generate other types of secondary radiation. A photon entering the sensitive part of detectors normally encounters and transfers electromagnetically all its energy E_{ph} to an atomic photoelectron. Depending on a

Nuclear Electronics with Quantum Cryogenic Detectors, Second Edition. Vladimir Polushkin.

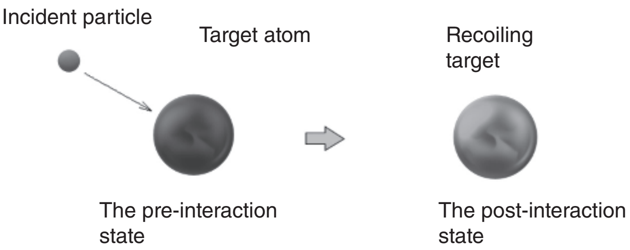

Figure 1.1.1 Schematic representation of the nuclear particle absorption process.

value of E_{ph}, the excited photoelectron can (i) raise to a higher bound state and generate secondary photons during the relaxation process, (ii) leave atom completely (the ionization) and initiate/participate in the energy conversion, and (iii) stay in the original bound state, but generate phonon particles that, in the case of superconductors, contribute to the Cooper pair-breaking process or generate informative heat in normal metal calorimetric absorbers. The phenomenon is often referred to as *the photoelectric effect*. We will return to it in Section 1.3.1.

As we mentioned earlier, some of charged particles and neutrons in the incident beams come very close to target nuclei that may result in the nuclear particle reactions. One can distinguish between two types of nuclear reactions: (i) interaction of incoming particles with nucleons and (ii) penetration of incoming particles into the target nuclei (the radiative capture). Both nuclear reactions leave the recoil nuclei in an excited state, which subsequently relaxes by emitting new particles or/and transmutation into different nuclear species. The secondary nuclear reaction products, i.e. photons and charged carriers, can be measured by radiation detectors. For that, they are built as "sandwiches" including nuclear reaction layers on top of or in the middle of the sensing device absorber. Provided that the nature of nuclear reactions involved is known, measurement data from the secondary sensor can be used to restore information about the primary particles of interest. We will give more details on that in Section 1.3 when we talk about detecting neutrons and in Chapter 4 when we discuss WIMP hybrid semiconductor – transition edge sensor (TES) detectors.

The scattering interactions are characterized by the fractional energy and/or momentum exchange between particles and recoiling targets. In these interactions, particles themselves exist as independent objects before and after collisions. Sometimes, the absorption process of a particle by, e.g. nucleus, which is followed by subsequent expel of the same particle or another similar particle, is also referred to as scattering.

Figure 1.1.2 demonstrates two types of scattering interactions. In *the elastic scattering* (Figure 1.1.2a), the total kinetic energy of a particle and a participating target does not change before and after collisions. The collisions, in which the kinetic energy is channeled down to the excitation of target atoms, are referred to as *the inelastic scattering* (Figure 1.1.2b). In both cases, the strong Coulomb forces of target atoms divert the initial trajectory of collided particles by a succession of angles, which are called *the scattering angles*.

With these basic definitions, we can now discuss selected aspects of primary nuclear reactions in more detail. The generic scope of this topic is simply enormous. There are multiple nuclear physics manuscripts dedicated to it. A lot of useful quantitative information can be found, for instance, in the books and scientific papers on the particle probe analytical chemistry. The modern computation power has brought the Monte Carlo simulation routine to every laboratory. The passage of radiation through matter can now be modeled by dedicated particle physics software toolkits, like GEANT4 [1]. Modern software is very advanced in terms of computation accuracy and input interface. It should take care of the majority of possible nuclear reactions and interaction mechanisms. Still, the researchers and engineers must have a detailed understanding of models employed to give the right interpretations to the simulation results and make sure simulated data does not under-/overshoot the expected ballpark values due to the code instability.

Section 1.1 will define the intrinsic quantum efficiency (IQE) of the radiation detectors. The following text will be structured around selected aspects of particle interaction with solid-state absorbers to characterize detectors in terms of the collection efficiency, required geometry, transport mechanisms, etc. It is essential for the quantitative measurements with radiation detectors to either contain the full energy deposited by an incoming beam or at least a well-known part of it to be able to deliver accurate results. Section 1.2 will deal with charged particles. We will differentiate between the light and heavy particles and define their penetration depth depending on their energies. Section 1.3 will focus on the photon measurements. The detection of neutrons and WIMPs will be the subjects of Sections 1.4 and 1.5, respectively.

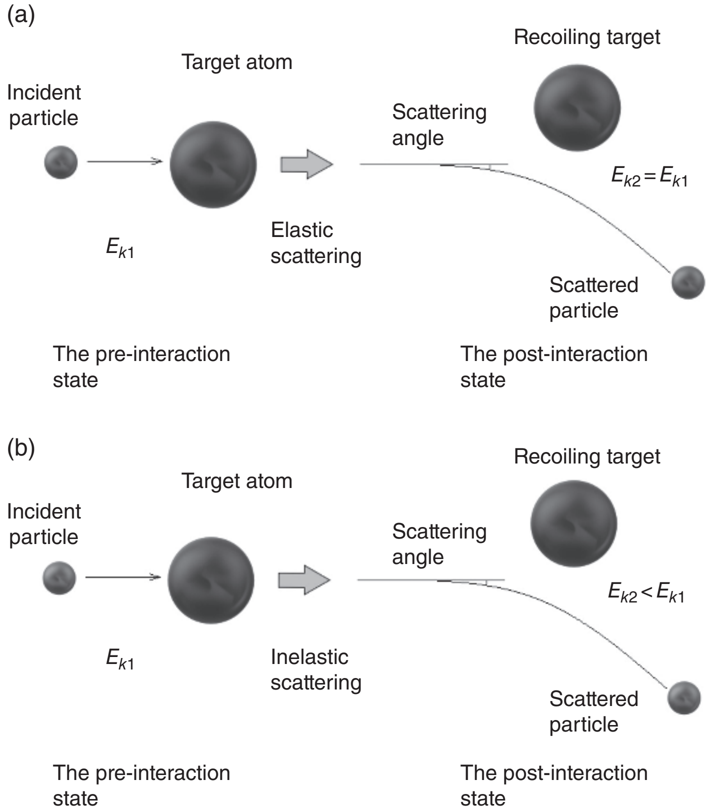

Figure 1.1.2 Two types of scattering interactions between the incoming particle and the target atom. (a) The kinetic energy of the particle in the elastic scattering does not change before and after collisions. (b) In the inelastic scattering, the kinetic energy is partially channeled toward the excitation or ionization of the atom.

1.1 The Intrinsic Quantum Efficiency of Radiation Detectors

The IQE can be defined in general terms as the percentage of incident nuclear particles that the absorber converts into informative charge carriers sampled by sensing device [2]. For the first phase of the detection process, as outlined in the Introduction earlier, the quantum efficiency (QE) is quantified by *the intensity attenuation function* and *the incomplete charge collection*. The attenuation function is defined as

$$\alpha_{ATT} = I(t_{abs})/I_0 \tag{1.1.1}$$

where I_0 and $I(t_{abs})$ represent intensities of the incident radiation beam and radiation passed through the absorber without interaction, respectively, and t_{abs} denotes the thickness of the absorber. By the intensity of radiation, we mean the number of nuclear particles passing through a unit area per unit time (the beam current). The IQE depends on the type of radiation, energy distribution in the beam, absorber material, and its geometrical dimensions.

Provided that each particle in the beam current transfers its energy in a single collision and then disappears (the absorption process), the intensity attenuation function takes the following form:

$$\alpha_{ATT} = \exp\left(-t_{abs}/\lambda_{abs}\right) = \exp\left(\mu_{abs} t_{abs}\right) \tag{1.1.2}$$

where μ_{abs} is the absorption coefficient reciprocal to the linear attenuation factor λ_{abs}. Both μ_{abs} and λ_{abs} are tabulated for the majority of materials utilized in radiation detectors (see, for instance [3]).

The majority of incoming charged particles tend to relax through multiple scattering events before they disappear from the beam. Therefore, appropriate correction factors must be introduced in Eq. (1.1.2) to take into account the difference in behavior. We will discuss these corrections in the following sections.

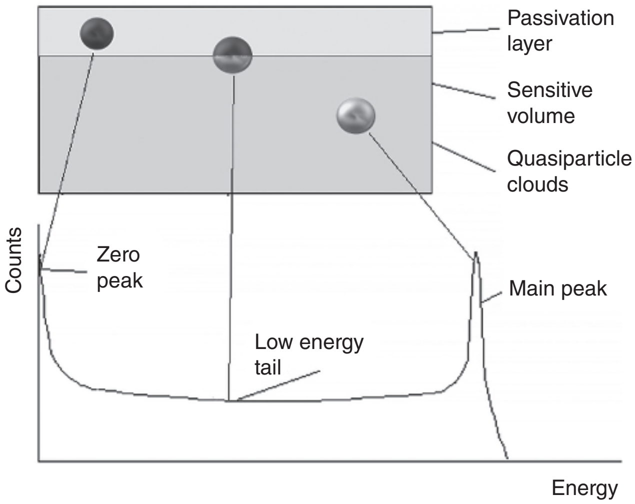

Figure 1.1.3 The low energy tail originated from the splitting of the quasiparticle energy down-conversion spheres between the passivation/insulation layer and the sensitive volume of the absorber. The down-conversion processes located wholly in the passivation and the sensitive volume contribute to the zero and main peaks, correspondingly.

The incomplete charge collection takes place in all three phases of the detection process. One mechanism, relevant to the primary nuclear reaction (the phase 1 under consideration), relates to the splitting of electron clouds formed by the energy down-conversion channels. The clouds get divided between the sensitive part of the absorber and the surface passivation or the gate insulation layer. Figure 1.1.3 illustrates this mechanism. The interaction spheres located wholly in the sensitive volume of the absorber contribute to the desirable main peak of the energy spectrum. Since the insulation materials have large energy gaps, the passivation layer normally generates significantly fewer nonthermal quasiparticles than the absorber material. Therefore, divided interaction spheres contain a partial amount of charge carriers. They contribute to the low energy tail that needs to be minimized. The spheres situated entirely in the passivation layer tend to form near-zero peaks.

Concerning photons, their density absorbed by the passivation layer N_{abs} can be evaluated using (1.1.2) as

$$N_{abs} = N_{ph}\left[1 - \exp\left(\mu_{pl} t_{pl}\right)\right] \tag{1.1.3}$$

where N_{ph} is the photon density in the original beam and μ_{pl} and t_{pl} denote the absorption coefficient and thickness of the passivation layer. Again, Eq. (1.1.3) should be adapted for the charged particle beams.

1.2 Detection of Charged Particles

As mentioned in the introduction, the inelastic collision of a charged particle with a valence electron in the target atom results in either the direct ionization or excitation of the atom. The excitation may elevate bound electrons to higher energy shells in the valence band, whereas the ionization removes at least one of them from the atom completely creating a free electron–hole pair. In other words, direct ionization takes place if a charged particle transfers to the valence electron energy that exceeds the ionization potential of the atom in the affected covalent bond (in the case of the covalent semiconductors). The actual energy transfer is mediated by electromagnetic fields surrounding the interacting atoms. Due to the long range of the electromagnetic forces (mainly the electric Coulomb force that decays as $1/r^2$, with r being the distance between particles), the ionizing interactions may occur even when the incident particle does not pass the target atom in close proximity. The kinetic energy of freed electrons is estimated as

$$E_{el} = E_t - \Delta \tag{1.2.1}$$

where E_t is the energy transferred to a valence electron as a result of the inelastic collision and Δ is the binding (or gap) energy. E_{el} can be sufficient for the freed recoil electrons to initiate subsequent chains of excitation and ionization events. Secondary electrons are essentially light-charged particles themselves with similar physics behind their relaxation process.

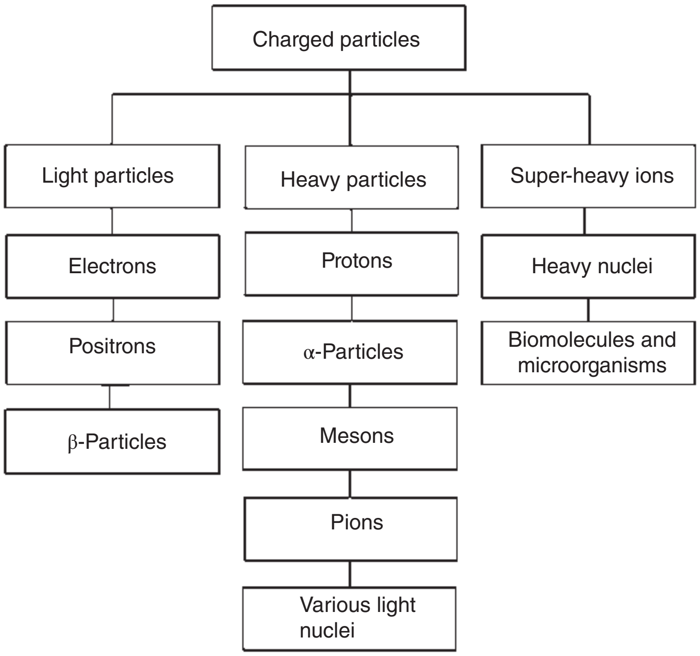

Figure 1.2.1 The classification of charged nuclear particles.

Charged particles with energies below the atom ionization potential can still produce a measurable amount of informative quasiparticles through the phonon generating mechanism in the superconducting (athermal) and normal metal absorbers attached to low-temperature detectors (thermal hot electrons).

Conditionally, all charged particles can be divided into three groups [4]. The first group comprises light particles, e.g. electrons, β-particles, and positrons. The second group includes heavy-charged particles, such as protons, α-particles, heavy ions, mesons. Super-heavy ionized biomolecular particles and microorganisms constitute their separate group. Figure 1.2.1 summarizes the classification in a diagram form. In the figure, we distinguish the electron from the β-particle to emphasize its dual nature. The term "β-particle" refers to an electron specifically released from nuclei.

1.2.1 Light-Charged Particles

The inelastic collisions of light-charged particles with absorber media produce a series of characteristic radiations. These are as follows:

- The secondary electrons;
- The Auger electrons;
- The diffracted electrons;
- The backscattered electrons;
- The characteristic X-rays;
- The bremsstrahlung (braking radiation);
- Others.

Figure 1.2.2 gives a schematic illustration of the primary and secondary volumes in which incoming charged nuclear particles interact with a radiation detection absorber. The drawing also defines sub-volumes where specific nuclear reactions generate each of the previously listed characteristic products. Calling the radiations' "characteristic" means that they contain important information about the physical properties and chemical composition of the target material. They are fundamental for multiple nuclear analytical methodologies and tools used widely in electron microscopy, chemical analysis, crystallography, medicine, radiometry, etc. The majority of these analytical instruments utilize the semiconductor and superconductor radiation sensors, which we will discuss in the following chapters of this manuscript, due to their superior performance specifications.

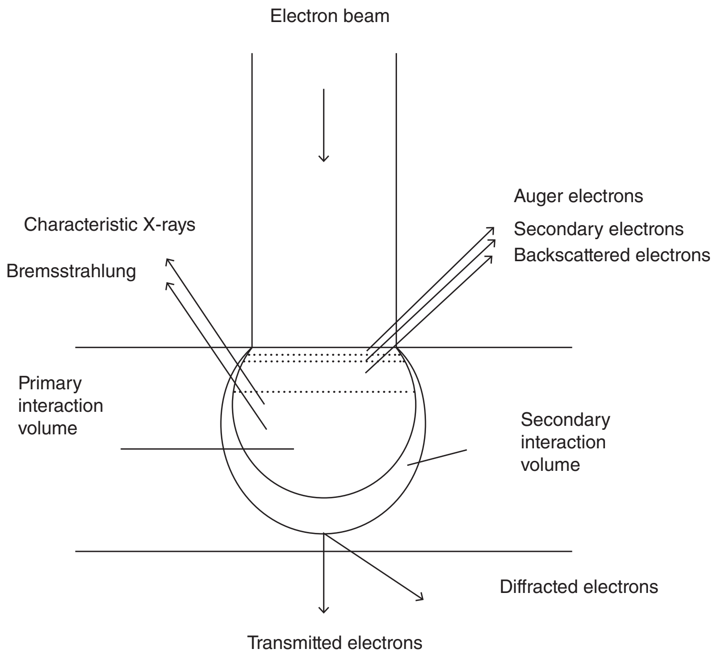

Figure 1.2.2 A schematic visualization of primary and secondary volumes where the interaction of incoming charged nuclear particles with radiation detection absorber takes place.

Since the cryogenic detectors demonstrate sensitivity to all types of radiations, the light-charged particles bombarding the detection medium of sensors excite similar characteristic products in the absorber's sensitive volume itself, as shown in Figure 1.2.2. These excitations borrow energy from main informative peaks, give rise to additional (unwanted) peaks, absorption minimums, low energy tails, backgrounds, and other traces in the radiation spectrometer output on the acquired energy spectrum diagram. Therefore, a good understanding of all nuclear reactions in a particular absorber's material of choice is absolutely important for achieving high accuracy in the radiation measurements. Modeling the detector response can assist in selecting the right absorber type, optimization of the overall detector design, and developing the appropriate mathematical models to introduce corrections to the acquired raw data.

At the very beginning of the energy down-conversion cascade, the incident charged particles tend to lose their energy (if it is above a few keV) mainly through the long-range collisions with target atoms and continuous radiation (bremsstrahlung). Then, the quasiparticle generation process proceeds through multiple chains of the energy partitions between electron–electron short-range and electron–phonon longer-range interactions. At the end of the relaxation process, the athermal detector absorber should contain quasiparticles with an informative density $\langle N_{qp} \rangle$ that correlates with the energy deposited by incident events. Various energy loss mechanisms, including all the characteristic radiation products plus the energy stored in the phonon system at the end of the down-conversion, influence the major detector performance specifications, e.g. ε_{qp} and F. Here, ε_{qp} is the average energy required to generate a single informative quasiparticle (often referred to as the ionization potential in semiconductor detectors), and F denotes the Fano factor. ε_{qp} and F define the statistical intrinsic energy resolution (see Chapter 2). Some of the characteristic radiations, especially bremsstrahlung, contribute significantly to the background noise, further limiting the resolving power of detectors.

1.2.1.1 Attenuation Function for Charged Nuclear Particles

Now, we will give an estimate for the IQE of absorbers intended to capture the charged particles and transform their energy into informative quasiparticles collected by the charge-sensitive preamp either directly or through the attached sensing devices, e.g. superconducting tunnel junctions. As we mentioned before, charged particles undergo multiple elastic and inelastic collisions, in which they correspondingly lose only fractions of their energies remaining in the beam for some time (see Figure 1.2.3). The penetration depth for each particle varies, but, statistically, there exists an average propagation distance over the ensemble, which is usually referred to as *the range*, R. At the end of the straight-line length, R, particles are assumed to be statistically relaxed to the thermal equilibrium. In terms of the quasiparticle response to the incoming

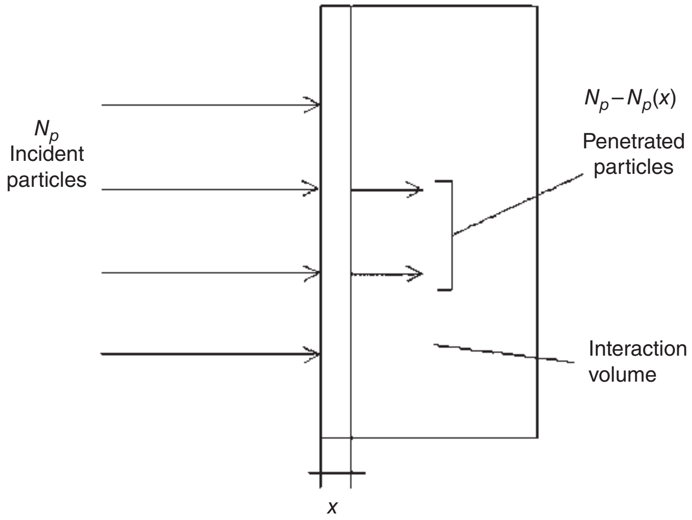

Figure 1.2.3 Penetration of particles into the interaction medium of a solid-state radiation detector.

charged particle itself, a specifically defined *ionization range* can be of interest. The ionization range characterizes particle trajectories from a point with an initial energy E_p to a point where the particle relaxes to a threshold energy level of ~$3/2\Delta$ so that one final scattering from the valence electron removes it from the beam. The attenuation function can then be approximated either by the shifted exponent, i.e.

$$\begin{aligned} I &= I_0 \quad \text{at } 0 < x < R \\ I &= I_0 \exp\left[-(x-R)/\lambda_{abs}\right] \quad \text{at } x > R \end{aligned} \tag{1.2.2}$$

or the Gaussian function (see, for instance [5]). In the latter case, R represents the mean value of the distribution at the half maximum, as shown in Figure 1.2.4. A statistical distribution of R is often referred to as *the range struggling*.

For simplified ballpark evaluations, one can use a semiempirical formula for the mean range given by [4]:

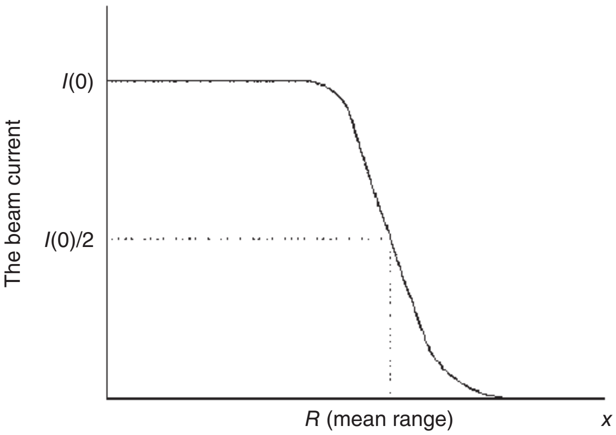

Figure 1.2.4 Radiation intensity as a function of the charged particle penetration depth. R represents the mean penetration range of the radiation.

$$R(E_p) = R(E_{min}) + \int_{E_{min}}^{E_p} \left(\frac{dE}{dx}\right)^{-1} dE \tag{1.2.3}$$

In this equation, E_{min} is the minimum energy at which the Bethe–Bloch theoretical modeling is valid. For incoming charged particles with energies above a few keV, the Bethe–Bloch formula for the linear energy transfer as a function of the penetration depth, x, is given by [5]

$$\left(\frac{dE}{dx}\right)_{inel} \approx 2\pi N_a r_e^2 m_e c^2 \rho \frac{Z}{A}\frac{1}{\beta^2}\left[\ln \frac{e_k^2(e_k+2)}{2\left(\frac{I_p}{m_e c^2}\right)^2} + F(e_k) - \delta - 2\frac{C}{Z}\right] \tag{1.2.4}$$

with N_a being the Avogadro number, A and ρ are the atomic mass and density of the detection medium, Z is the atomic number, $r_e = 2.817 \times 10^{-13}$ cm is the classical electron radius, $m_e = 9.108 \times 10^{-31}$ kg is the rest mass of an electron, c is the velocity of light, $\beta = \frac{v}{c}$, $e_k = \frac{E_k}{m_e c^2}$ denote the dimensionless reduced velocity and the kinetic energy of the incident particle, respectively, I_p is the mean excitation potential, and δ, C represent the density and shell correction factors. Since the masses of interacting objects in the inelastic scattering are almost the same (not true for relativistic particles), the maximum energy transfer per collision cannot exceed half of the kinetic energy of the incident charged particle. Thus, the function $F(e_k)$ takes the following forms:

a) For electrons and β-particles,

$$F(e_k) = 1 - \beta^2 + \frac{\frac{e_k^2}{8} - (2e_k + 1)\ln 2}{(e_k + 1)^2} \tag{1.2.5}$$

b) For positrons,

$$F(e_k) \approx 2\ln 2 - \frac{\beta^2}{12}\left(23 + \frac{14}{e_k + 2} + \frac{10}{(e_k + 2)^2} + \frac{4}{(e_k + 2)^3} + \ldots\right) \tag{1.2.6}$$

For those who prefer even simpler solutions, an empirical expression has been derived for a case of $E > E_{min}$ [6, 7]:

$$R(\mu\text{m}) \approx \frac{2.76 \cdot 10^{-2} A E_0{}^{1.67}}{\rho Z^{0.89}} \tag{1.2.7}$$

Equation (1.2.7) provides adequate accuracy for the detector efficiency evaluation in an energy range of 10–1000 keV.

For light-charged particles with energies 10 eV < E_p < 10 keV, the total number of collisions per particle is insufficient to justify the usage of the Bethe–Bloch statistical formalism. The energy loss in solids can be estimated using the Lindhard dielectric response of a medium to a passing particle transferring its kinetic energy $\hbar\omega$ and changing its momentum by $\hbar k$ on its way [8, 9]. The mean range for continuous energy loss from E_p ~ 10 keV to 10 eV is given by [10]:

$$R(E_p) = \int_{10\ \text{eV}}^{E_p} \frac{1}{S(E)} dE \tag{1.2.8}$$

where $S(E)$ is the energy loss per unit path length or stopping power of the absorber material. Calculated $R(E_p)$ and $S(E)$ for 58 elemental materials including those that are normally used in radiation detectors are published in Tanuma et al. [11, 12]. Figure 1.2.5 gives an example of the mean range as a function of charged particle energy $R(E_p)$ in a range from 50 eV to 5 keV calculated using data from Tanuma et al. [11].

An average nucleus diameter is only a 10^{-5} fraction of the atom size. The remaining volume is occupied by the orbital electrons (electron gas). This implies that the probability for a charged particle to interact with a nucleus in the close-range collision (nuclear reaction) is much smaller compared with the probability of interaction with valence electrons. For silicon, scatterings from the valence electrons represent the major loss mechanism at the electron energies from 10 eV to 10 keV. Below 10 eV, ionization collision rate drops exponentially reaching a value of 5×10^{10} s^{-1} at 2 eV. Further relaxation is dominated by the fast inelastic electron–phonon interactions.

It is important to reemphasize again that these computations are normally performed with dedicated design/simulation tools. Giving these equations, we are not trying to advocate performing calculations in the old-fashioned style. We rather highlight the point that all simulation tools employ specific models that have their limitations. Engineers can only rely on them if all issues complicating the analysis and the applicability of built-in models for achieving correct results are well understood.

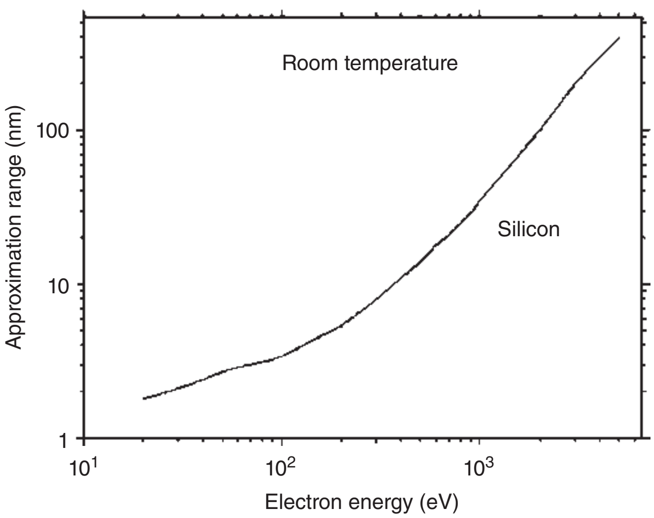

Figure 1.2.5 A plot of the mean range as a function of charged particle energy $R(E_p)$ in a range from 50 eV to 5 keV calculated using data from Tanuma et al. [11].

1.2.2 The Continuous "Braking" Radiation (Bremsstrahlung)

The long-range Coulomb forces of nuclei exert a strong influence on charged particle tracks. Even elastic scattering events affect detector quantum efficiency. They divert particles from their original direction causing bremsstrahlung or backscattering of particles from the detector absorber. The interaction volume also emanates Auger electrons created as a result of the inelastic collisions near the entrance window region (Figure 1.2.2).

The charged particles decelerate primarily through the deflection by the nucleus's strong electric field (although the screening effect from valence electrons also plays its part in the process). A deflected particle loses some of its kinetic energy that is emitted as a breaking photon, i.e. $h\nu = E_p(before) - E_p(after)$. Here, $h\nu$ is the energy of the photon and $E_p(before)$ and $E_p(after)$ denote the particle kinetic energy before and after the deflection.

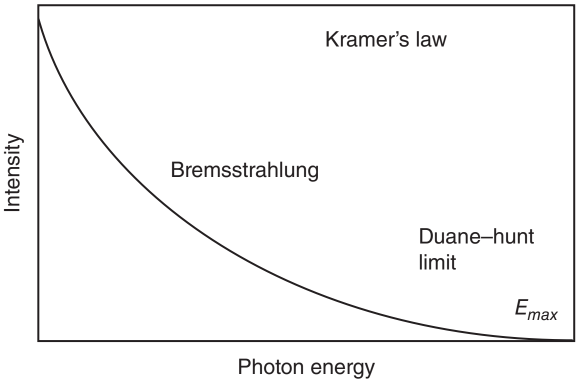

Figure 1.2.6 The distribution function of continuum photons caused by bremsstrahlung.

Free electrons and positrons do not have discrete allowed energy levels. Therefore, the "braking" radiation has a continuous energy spectrum extending from near-zero to the maximum energy of incoming charged particles minus the binding energy Δ of the absorber material. Since the emitted deceleration photons generate an increasing number of free carriers with progressively smaller energies, their continuum distribution function has a shape as shown in Figure 1.2.6. The curve was derived from the Kramer's equation for the intensity in photons per second per unit energy interval per incident electron [13]:

$$N_{brem}(E) = 2 \times 10^{-9} Z \frac{E_p - E}{E} \tag{1.2.9}$$

where E is an energy of interest.

The partition of the total stopping power of the material $\left(\frac{dE}{dx}\right)_\Sigma$ between $\left(\frac{dE}{dx}\right)_{col}$ due to inelastic collisions and $\left(\frac{dE}{dx}\right)_{brem}$ due to bremsstrahlung varies with energy. In the low energy range, particles tend to relax mostly via inelastic scattering from atom electrons, i.e. $\left(\frac{dE}{dx}\right)_\Sigma \to \left(\frac{dE}{dx}\right)_{coll}$. At very high energies, the energy loss is dominated by bremsstrahlung, i.e. $\left(\frac{dE}{dx}\right)_\Sigma \to \left(\frac{dE}{dx}\right)_{brem}$. Contributions from both mechanisms must be taken into account for charge particles accelerated to intermediary energies. There is a crossover energy E_c at which these contributions become equal, $\left(\frac{dE}{dx}\right)_{coll} = \left(\frac{dE}{dx}\right)_{brem}$. For the interaction of electrons with semiconductors, a crossover point $E_c \sim$ few tens of MeV.

Bremsstrahlung manifests itself as a background continuum on the energy spectrum histogram. An example of such a diagram experimentally obtained from the pure bulk silicon is shown in Figure 1.2.7. The X-ray attenuation at low energies seemingly opposes the Kramer's function. In reality, this results from photon absorption by matter. These photons exist but simply do not reach the detector measuring the X-ray irradiation. To demonstrate the intensity of the braking radiation, Figure 1.2.7 also includes a strong Si K_α characteristic peak. One can see that a part of the peak is smeared. The background continuum may mask completely some of the lower-intensity signals generated by the measured radiation. It also complicates the separation of closely spaced peaks on the energy spectrum. Both problems become particularly serious in the low-energy region.

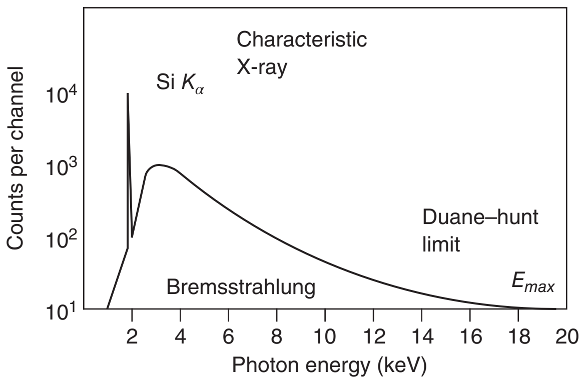

Figure 1.2.7 Bremsstrahlung manifests itself as background continuum on the energy spectrum histogram. Low energy attenuation as opposite to the Kramer's function is due to the photon absorption by matter.

1.2.3 Backscattering of Charged Particles

The deflection of charged particles from their original directions by the Coulomb forces of nuclei with strong field gradients has other implications on the detection process besides

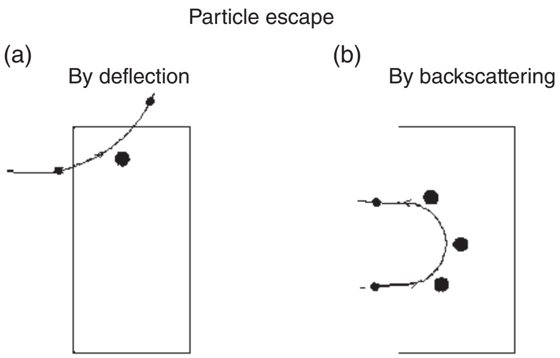

Figure 1.2.8 (a) A large-angle scattering event near the edge diverts an incoming particle out of the detection volume before its relaxation has been completed. (b) The backscattering effect when the total deflection angle becomes larger than $\pi/2$, so that the particle is ejected back from the detector front surface.

bremsstrahlung. Multiple elastic interactions shape propagation paths into meander-like forms that increase the interaction volume and can move it toward surfaces with a large density of trapping states. A large-angle scattering event near the edge can divert an incoming particle out of the detection volume before its relaxation has been completed (or even started). Figure 1.2.8a illustrates this case. A succession of several elastic collisions may lead to *the backscattering effect*. It happens when the total deflection angle becomes larger than $\pi/2$ so that the particle is ejected back from the entrance window of the detector. The backscattering effect is illustrated in Figure 1.2.8b. Free electrons produced by the ionization process can also escape from the detector as the secondary and Auger electrons. To be able to leave the detection volume, their energies need to be larger than the surface work function, F_w, of the surface material (or materials if the entrance window contains several layers). By convention, only electrons with energies below 50 eV emitted from a depth less than 1 nm are referred to as secondary. They are distinguished from others, more energetic electrons that can come out from a depth up to 50 nm.

The backscattering process is normally quantified by *the backscattering coefficient*, which represents the fraction of the total number of incident particles that the detector emits back from the front surface to, i.e.

$$\eta_{bs} = I_{bs}/I_0 \tag{1.2.10}$$

The coefficient depends on the atomic number of the medium. For all elemental materials used as radiation absorbers, η_{bs} increases as the particle energies become lower. High energy particles tend to penetrate deeply into the medium ($R > 50$ nm) where even scattered at high angles they can be reabsorbed efficiently by the lattice.

The backscattering of particles out of the detection volume before they have relaxed to below Δ leads to *the charge collection deficit*. It affects the low energy quantum efficiency of detectors. In addition, the incomplete charge collection marks its presence through the shift and broadening of major informative peaks on the energy histogram. It also adds spurious peaks and voids to the bremsstrahlung continuum.

1.2.4 Heavy-Charged Particles

The class of heavy-charged particles incorporates all elementary particles with masses exceeding the electron mass, i.e. protons, α-particles, muons, pions, light nuclei, etc. The principle behind their interaction physics with solid-state absorbers is similar to that of electrons and positrons that we analyzed in Section 1.2.1. Thus, in addition to what was discussed, we only need to introduce some quantitative corrections into equations describing the energy channeling process.

The initial velocity of a heavy-charged particle is approximately $\sqrt{\frac{M}{m_e}}$ times lower than the velocity of the electron with the same energy (M is the mass of a heavy particle under consideration). This reduction in the velocity extends the interaction time between particles and atoms, which leads to increased energy loss per collision. The valence electrons of interacting target atoms have enough time to acquire energy close to a maximum value that is evaluated as [14]

$$E_{max} = \frac{2m_e c^2 \eta^2}{1 + 2s\sqrt{1 + \eta^2 + s^2}} \tag{1.2.11}$$

where $s = \frac{m_e}{M}$, $\eta = \beta\gamma$, $\gamma = \frac{1}{\sqrt{1-\beta^2}}$. More efficient inelastic scatterings have two positive consequences for detector designers: (i) the range of heavy-charged particles becomes shorter and (ii) better defined at the same time (reduced the range struggling).

Provided that $\beta > 0.1$, the Bethe–Bloch equation for the linear energy transfer has the following modified form [4]:

$$-\frac{dE}{dx} = 2\pi N_a r_e^2 m_e c^2 \rho \frac{Z}{A}\frac{z^2}{\beta^2}\left[\ln\left(\frac{2m_e\gamma^2 v^2 E_{max}}{I_p^2}\right) - 2\beta^2 - \delta - 2\frac{C}{Z}\right] \tag{1.2.12}$$

where z is the charge of an incident particle in units of elementary electron charge, e_0.

Statistically, equally charged particles experience an average Coulomb deceleration force from nuclei, $\overline{F}_b$. This force is responsible for the braking radiation $\left(\frac{dE}{dx}\right)_{brem}$. The deceleration, $\overline{d}$, is inversely proportional to the square of the particle mass, M, i.e. $\overline{d} \sim \left(\frac{\overline{F}_b}{M}\right)^2$. This means that the relative contribution of $\left(\frac{dE}{dx}\right)_{brem}$ to the total stopping power reduces in proportion to $\frac{1}{M^2}$ as well. In other words, the inelastic scattering from valence electrons is the major energy loss mechanism for heavy-charged particles in a solid-state medium in the energy range up to a few GeV:

$$\left(\frac{dE}{dx}\right)_\Sigma \approx \left(\frac{dE}{dx}\right)_{coll} \tag{1.2.13}$$

Intuitively, the path of a heavy particle in the matter should be less perturbed by large-angle deflections compared with that of electrons or positrons. Indeed, collisions, in which particles can lose $\sim 4\frac{m_e}{M}$ fraction of their energy as a maximum, cannot incur any substantial scattering angle. The average scattering angle by the Coulomb forces from nuclei also has a downward trend in proportion to the square of the particle mass multiplied by the screening effect from surrounding electrons.

A quasi-straight track, the reduced mean free path (reciprocal to the number of collisions per unit length $\left(\sim \frac{1}{4}\frac{M}{m_e}\right)$ in total during the particle passage), and a better-defined energy loss rate per collision enable the range to be predicted with a very good accuracy using simple analytical expressions. Plots in Figure 1.2.9 present ranges of α-particles and protons in comparison with the electron ranges for Si (a) and Ge (b) absorbers. Similar plots for these particles in detector-sensitive volumes made of other materials can be evaluated following the empirical Bragg–Kleeman rule [15]:

$$R_{det} = \frac{\rho_{Si}}{\rho_{det}}\sqrt{\frac{A_{det}}{A_{Si}}}R_{Si} \tag{1.2.14}$$

where R_{det}, ρ_{det}, and A_{det} denote the range, density, and atomic weight of a detector medium of interest and R_{Si}, ρ_{Si}, and A_{Si} are the respective values for Si. In the case of compound material, A_{det} denotes an effective atomic weight, which is defined as

$$A_{det} = \left(\frac{\eta_1 A_1 + \eta_2 A_2}{\eta_1\sqrt{A_1} + \eta_2\sqrt{A_2}}\right)^2 \tag{1.2.15}$$

where η_1 and η_2 are the atomic fractions of chemical elements in the compound with atomic weights A_1 and A_2.

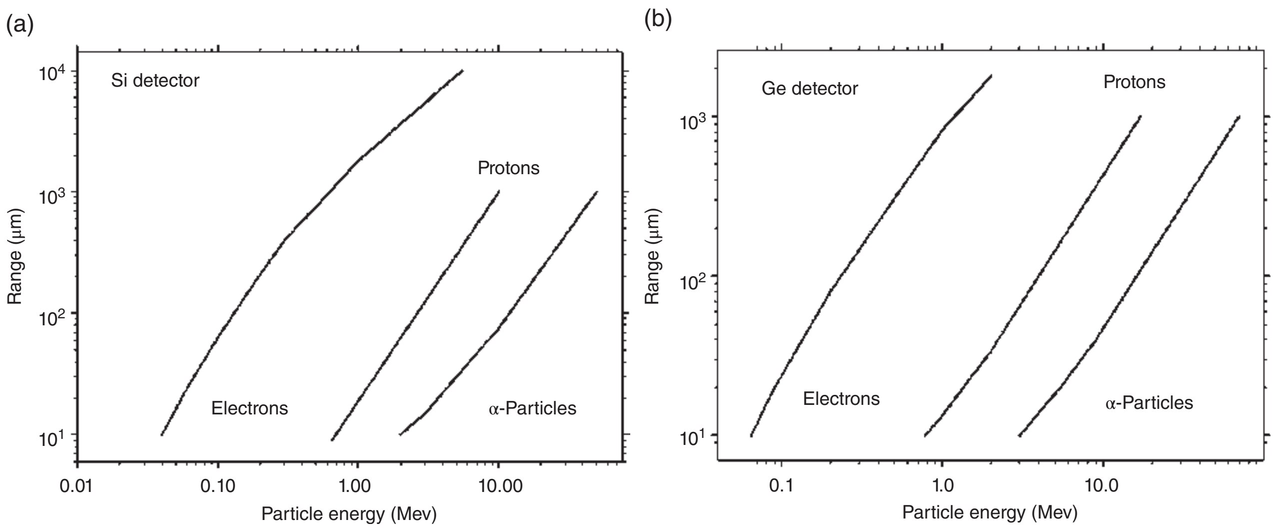

Figure 1.2.9 Range of heavy particles as a function of their energy for Si (a) and Ge (b).

Some low-energy particles charged positively (including those that lost their energy in collisions) can attract free electrons from the medium for some period of time and, thereby, using their screening effect propagate much deeper in the absorber as a quasi-neutral particle. This may result in the charge collection deficit if particles leave the interaction volume before the thermalization process is completed. The phenomenon is particularly pronounced in the normal metal and superconducting absorbers. In semiconductor detectors, interaction volumes are depleted of free carriers. Therefore, positive charge particles can only attract electrons unbounded as a result of their inelastic scattering events. This means that the phenomenon is influenced by the energy of incoming particles and the beam intensity.

1.3 Primary Interactions of X- and γ-Ray Photons with Solid-State Absorbers

The dual nature of matter becomes particularly evident when we deal with the light. Infrared, visible light, ultraviolet, X-rays, and γ-rays demonstrate wavelike phenomena such as interference, diffraction, and polarization. At the same time, we treat them as photon particles (i.e. packets of electromagnetic waves), to explain the following quantum mechanical effects:

1) The photoelectric effect;
2) The Compton scattering;
3) The pair production.

These effects represent the major interaction mechanisms between photons and absorber materials. They also constitute the base for the X- and γ-ray detection methodologies. Since photons have no charge, the listed above three effects initiate indirect ionization energy cascades by the ejection of energetic primary photoelectrons. After that, the primary photoelectrons start participating in the energy down-conversion process similar to the process initiated by the light-charged particles discussed in Section 1.2. In this respect, there is no need to repeat the analysis of the complete interaction routine. We will focus primarily on the primary nuclear reaction mechanisms.

1.3.1 Photoelectric Effect

The photoelectric effect takes place at the absorption collisions between incoming photons and target atoms. At the first collision, photons tend to transfer all their energies E_x and momentums M_{ph} to the target atoms and disappear from the beam. The absorbed photon energy is then forwarded to one of the bound electrons, whereas the nucleus captivates the recoil momentum, as shown in Figure 1.3.1a. Provided that the condition $E_x > E_j$ holds, the atom ejects a photoelectron with kinetic energy given by

$$E_e = E_x - E_j \tag{1.3.1}$$

where E_j is the binding energy of the jth shell.

Figure 1.3.1b shows the case of $E_x \gg E_k$ when the outgoing electron leaves the inner K shell of the atoms. This energetic photoelectron initiates a subsequent ionization (or the pair breaking in a case of superconducting absorber) energy cascades. The remaining two diagrams of Figure 1.3.1c,d illustrate the de-excitation process in the atom in which the electron structure rearranges itself to occupy the lowest energy states available. The transitions from L shell to K shell and from M shell to L shell are followed by emission of characteristic X-rays with the following energies:

$$E_x' = E_k - E_l \tag{1.3.2}$$

$$E_x'' = E_l - E_m \tag{1.3.3}$$

The characteristic X-rays may participate in their own photoelectric interactions followed by corresponding down-conversion processes. This means that a radiation detector exposed to a monochromatic X- and γ-ray beam produces an energy spectrum enriched by multiple peaks from characteristic X-ray emissions. The overall energy of these peaks together with other artifacts discussed in Section 1.2 is borrowed from the main informative peak at the photon energy E_x. To improve measurement accuracy the borrowed energy deficit needs to be returned back to the E_x line by applying appropriate correction factors derived, e.g., from the Monte Carlo modeling.

The chain of possible photoelectric events lasts until energies of remaining photons and energetic quasiparticles become insufficient to free inner shell valence electrons. If the photoelectric effect is the only primary interaction mechanism

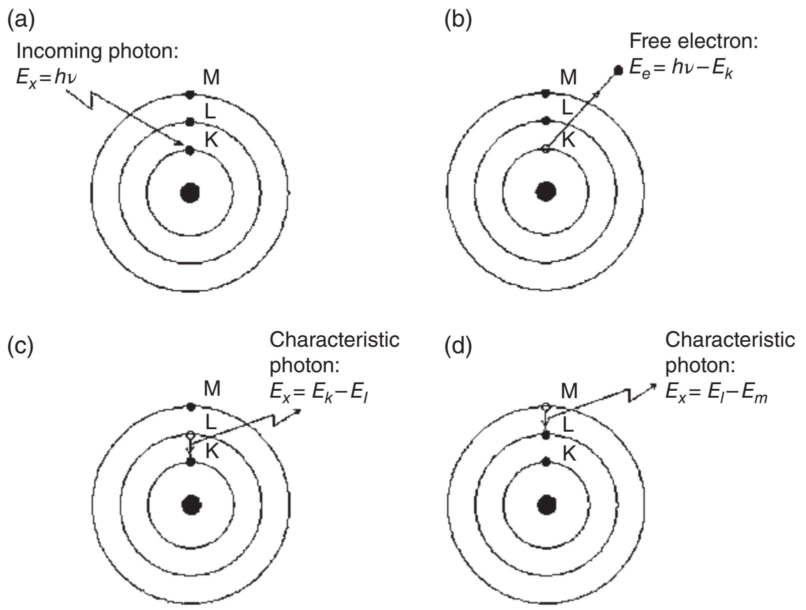

Figure 1.3.1 The shell diagrams illustrating X-ray photon interaction with the target atom through the photoelectric effect. (a) The photon transferring all its energy to the k-shell electron; (b) the electron with kinetic energy $E_x - E_k$ vacates the k-shell of the atom; (c and d) the electron structure rearrangement with the characteristic X-rays emissions.

between photons and the medium, the combined energy of photoelectrons approaches very close to the energy of incoming particles, i.e.

$$E^e_\Sigma \approx E_x \tag{1.3.4}$$

Equation (1.3.4) represents the necessary condition that defines the accuracy of solid-state radiation detectors with regard to X- and γ-ray measurements [16]. A generic example of a corrected photoelectric spectrum is presented in Figure 1.3.2. More information on mathematical modeling of the photon interaction with matter can be found in literature discussing the X-ray probe analysis techniques and description of the specialized simulation software, e.g. GEANT4.

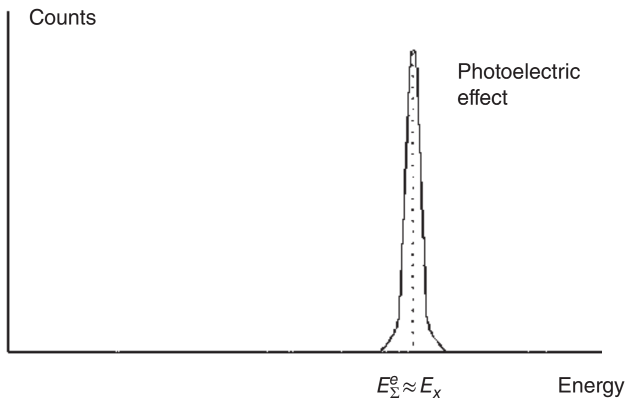

Figure 1.3.2 An energy spectrum representing the corrected primary photoelectric effect.

1.3.2 Compton Scattering

The photoelectric effect is more common for relatively low-energy X-rays. In the middle of the X- and γ-ray energy range, some of the incoming photons relax via inelastic scatterings from outer loosely coupled atomic electrons. The phenomenon is named after Arthur H. Compton who was the first to observe and explain it in 1923 [17]. Figure 1.3.3 illustrates the essence of the Compton scattering mechanism.

Let us assume that an electron with a mass m_e rests just before the interaction event. Then, an incident photon with energy E_γ and momentum $\mathbf{k}_\gamma$ collides with the electron. This results in the electron recoiling with an energy E_e and momentum $\mathbf{k}_e$ and the photon scattered into a new state with

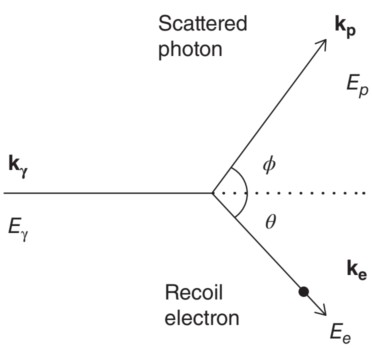

Figure 1.3.3 A schematic representation of the Compton scattering.

energy E_p and momentum $\mathbf{k_p}$. The conservation law of the energy and momentum given by

$$E_\gamma = E_e + E_p \tag{1.3.5}$$

$$\mathbf{k_\gamma} = \mathbf{k_e} + \mathbf{k_p} \tag{1.3.6}$$

suggest that the photon is scattered with a reduced energy $E_p < E_\gamma$ or increased wavelength $\lambda_p > \lambda_\gamma$ (according to the Planck relation: $E = h\frac{c}{\lambda}$, with h being the Planck constant and c is the light velocity). Compton discovered that the wavelength shift corresponds to

$$\lambda_p - \lambda_\gamma = \lambda_c(1 - \cos\theta) \tag{1.3.7}$$

where $\lambda_c = \frac{h}{m_e c}$ is the Compton wavelength.

Combining all three equations (1.3.5)–(1.3.7), the kinetic energy of the recoil electron takes the following form:

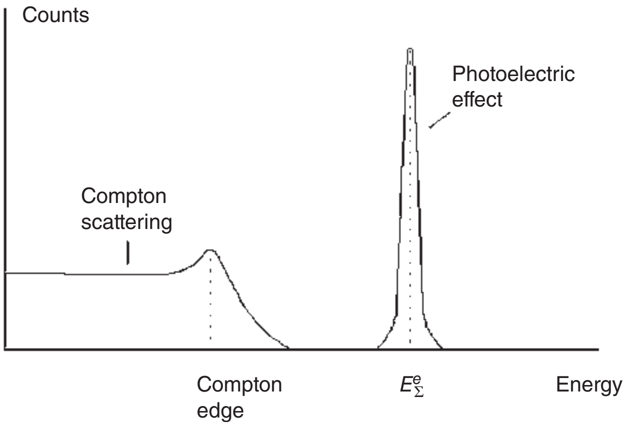

Figure 1.3.4 The Compton continuum on the energy spectrum diagram.

$$E_e = \frac{E_\gamma^2(1 - \cos\theta)}{m_e c^2 + E_\gamma(1 - \cos\theta)} \tag{1.3.8}$$

The scattering angle θ can be of any value from 0 to π. Therefore, a solid-state detector exposed to middle range X- and γ-rays will yield an energy spectrum that should look like a continuum extending from the zero line to the Compton edge. Figure 1.3.4 gives an illustration of the energy spectrum including the Compton continuum. The Compton edge corresponds to the maximum energy imparted from the backscattered incoming photon to the recoil electron ($\theta = \pi$), which is given by

$$E_e^{max} = \frac{2E_\gamma^2}{m_e c^2 + 2E_\gamma} \tag{1.3.9}$$

Unless the Compton scattering is informative (i.e. used as a detection method characterizing properties of incoming particles), it tends to degrade the detector performance. The continuum can mask low-intensity peaks in the range where it is pronounced and have a significant impact on the intensities and positions of photoelectric peaks borrowing energy from down-conversion channels that otherwise would contribute to the intensity of photoelectric lines in the histogram. On the positive side, the Compton scattering mechanism is well understood and quantified to very high accuracy. Modern quantum microscopic models are capable to deliver a set of high precision spectrum correction factors to reduce its influence on the final measurement result if necessary.

It is worth mentioning that in general the Compton effect may manifest itself in a more sophisticated form compared with the classical representation by Eq. (1.3.7). Depending on the material, the spectrum continuum can take various shapes and contain multiple peaks originating from associated subtle effects. We will not go deeply into this topic. Numerous dedicated papers and manuscripts discuss it in great detail. For example, interested readers can find a good overview of the subject in [18, 19].

The design and simulation tools should also incorporate more inclusive quantum mechanical models compared to Eq. (1.3.7). For a good accuracy of the analysis, it would be useful to take into consideration more realistic initial conditions, for instance, the fact that the atom electrons are not resting before and during the interaction events. Incoming photons interact rather with the plasma electron cloud around the target atoms (quasiparticles) rather than with standalone electrons. This means that excited quasiparticles can also transfer their kinetic energy to the low-energy photons and boost their energy levels. In this case, the right side of Eq. (1.3.7) takes the opposite sign implying that the wavelength of the outgoing photon becomes shorter. This phenomenon is also known as *the inverse Compton scattering*. For instance, infrared photons in collisions with relativistic electrons can be boosted well back into the X-ray region. The inverse Compton scattering also influences the detector performance. Some of the interaction electrons with $E > E_g$ restore ionization (pair breaking) capability of low energy photons, which otherwise would "quietly" relax through the phonon system. These boosted photons add counts to the background continuum in a way similar to bremsstrahlung.

1.3.3 The Pair Production

The pair production refers to the transformation of photons into the electron–positron pairs in the Coulomb field of nuclei. The transformation is illustrated in Figure 1.3.5.

The minimum energy required for this effect to take place is derived from the mass and energy conservation law, i.e.

$$E_\gamma \geq 2m_e c^2 + \frac{2m_e^2 c^2}{m_n} \tag{1.3.10}$$

where m_n is the mass of the target nucleus, $2m_e c^2$ is the combined rest mass–energy of the electron–positron pair. In practice, $m_n \gg m_e$, which enables the condition (1.3.10) to be rewritten in a simplified form as

$$E_\gamma > 2m_e c^2 \tag{1.3.11}$$

The excess energy $E_\gamma - 2m_e c^2$ is divided equally between the freed electron and positron. With this energy, both particles, if they stay inside the detector absorber volume, continue participating in the relaxation process similar to light-charged particles as discussed in Section 1.2.

The lifetime of the positron is quite short. Within 1 ns it is usually captured by electron clouds. Two anti-particles annihilate with the emission of two $m_e c^2$ photons in opposite directions. The process of the annihilation and reconversion into photons is illustrated in Figure 1.3.6a,b, respectively. The annihilation photons either relax in the interaction with medium electrons by the Compton and photoelectric processes or escape from the detection volume altogether. A spectral response example of the radiation detector exposed to high-energy γ-ray photons is presented in Figure 1.3.7. It contains three photoelectric peaks. The single escape and double escape peaks correspond to cases when one and both respective annihilation photons deposited all their energies in the detection volume through the photoelectric nuclear reaction.

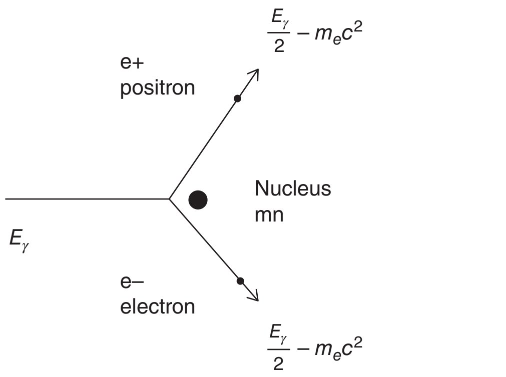

Figure 1.3.5 The pair production process. An incoming photon is transformed into the electron–positron pair in the Coulomb field of the nucleus.

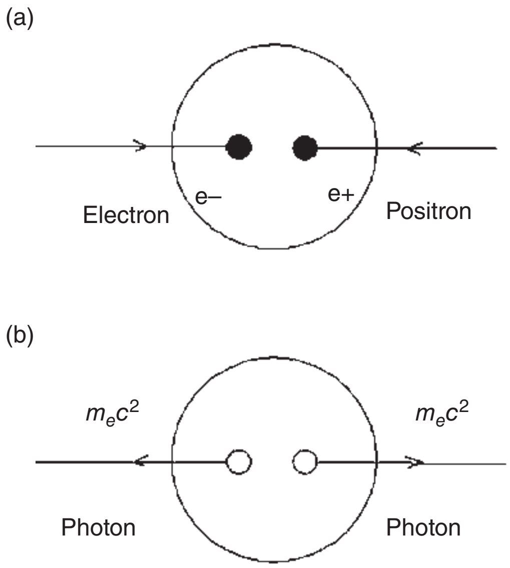

Figure 1.3.6 The process of electron–positron annihilation (a) and reconversion into photons (b).

1.3.4 Attenuation of Photon Radiation in Solid-State Detector Absorbers

Let us consider a case when the parallel beam of monoenergetic photons penetrates a detector absorber of a thickness, x, as shown in Figure 1.3.8. A fraction of incoming photons interacts with the medium, so that the intensity of the transmitted beam, I, is smaller than the intensity of the incident beam, I_0. If the energy absorption occurs by either the photoelectric effect or the pair production, photons transfer all their energy and disappear from the beam on their first interaction. In this case, Eq. (1.1.2) describes the transmission adequately. It can be rewritten in terms of beam intensities as follows:

$$I = I_0 e^{-\mu_\Sigma x} \tag{1.3.12}$$

where μ_Σ is the total linear attenuation coefficient. By definition, the total linear attenuation coefficient combines the individual attenuation coefficients for photoelectric, pair production processes, and the Compton scattering, i.e.

$$\mu_\Sigma = \mu_{ph} + \mu_{pp} + \mu_C \tag{1.3.13}$$

In doing so, however, one needs to remember that the Compton scattering does not remove a photon from the beam in a single collision. Similar to charged particles, photons relaxing via the Compton mechanism alone would have to be characterized by the range function similar to the charged particle treatment.

The interaction of particles with matter is often tabulated in terms of the individual or total cross sections. The cross section is defined as the interaction probability per target atom. Its relation to the linear attenuation coefficient is given by

$$\mu_\Sigma = \frac{N_a}{A}\rho\sigma_\Sigma \tag{1.3.14}$$

where $\sigma_\Sigma = \sigma_{ph} + \sigma_{pp} + \sigma_C$, σ_{ph}, σ_{pp}, and σ_C represent individual cross sections of the photoelectric, pair production, and Compton processes, respectively.

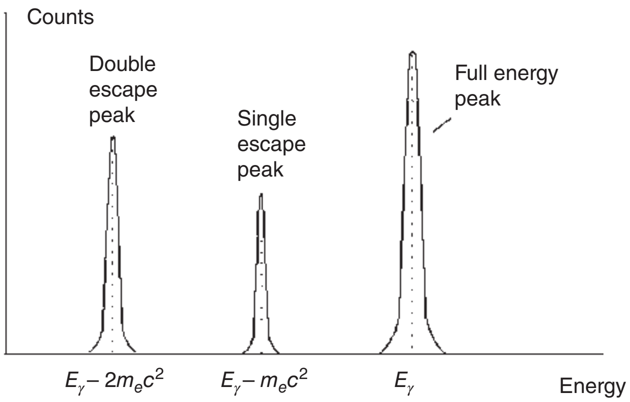

Figure 1.3.7 A typical spectral response of radiation detectors exposed to high energy photons initiating the pair production events. The histogram contains three photoelectric peaks. The single escape and double escape peaks correspond to cases when one and both annihilation photons escape from the detection volume without interactions, respectively.

1.4 Detection of Neutrons with Solid-State Radiation Sensors

The neutron is a fundamental particle with a mass of 1 amu, which equals approximately to the rest mass of 1839 electrons. The particle is electrically neutral and, therefore, not capable to directly ionize atoms via long-range Coulomb forces. Instead, penetrating the matter, it undergoes short-range interactions with atomic nuclei (nuclear reactions). For non-relativistic neutrons, one can distinguish three major types of nuclear reactions. These are as follows:

1) The absorption of neutrons by nuclei;
2) The elastic scatterings from nuclei;
3) The inelastic scatterings.

In the scattering collisions, the neutron imparts only a fraction of its energy and, thus, may interact with multiple target nuclei on its track. The nucleus converts the excitation energy received from the neutron into some form of radiative emission, e.g. X-ray, γ-ray photons, charged particle. If the thickness of the absorber permits, the reaction chain lasts until the particle either has been captured by a nucleus or disintegrates into a proton, β-particle, and neutrino at the end of its lifetime.

The total cross section (or the probability for particles to interact with the detector sensitive volume) includes all cross sections responsible for each nuclear reaction mechanism, i.e. [4]

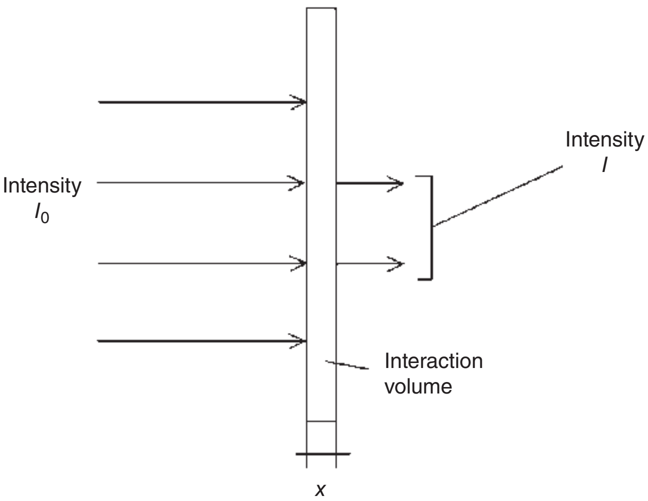

Figure 1.3.8 The interaction of a photon radiation beam with the solid-state absorber. I_0 and I represent the incoming and transmitted beam currents.

$$\sigma_{abs} = \sigma_{capture} + \sigma_{elastic} + \sigma_{inelastic} \tag{1.4.1}$$

It depends strongly on the kinetic energy, E_k (or velocity, v) of neutrons in the beam. For instance, the absorption probability increases in proportion to the time duration it spends in the close proximity (~10^{-15} m) with nuclei, i.e.

$$\sigma_{abs} \propto \frac{1}{v} \propto \frac{1}{\sqrt{E_k}} \tag{1.4.2}$$

This type of nuclear reaction is likely to be dominating for *slow* neutrons with $E_k < 1$ eV, while *fast* neutrons with $E_k > 100$ keV tend to transfer their energy predominantly via scattering mechanisms until they become *moderated* to an energy $E_k < 1$ eV.

Figure 1.4.1 presents a more complete classification of possible nuclear reaction types between neutrons and nuclei. The four mechanisms added to the absorption and elastic/inelastic scatterings make significant contributions for high energy (relativistic) particles. We will not be discussing them in this manuscript. Interested readers can find detailed information in specialized literature, e.g. [20].

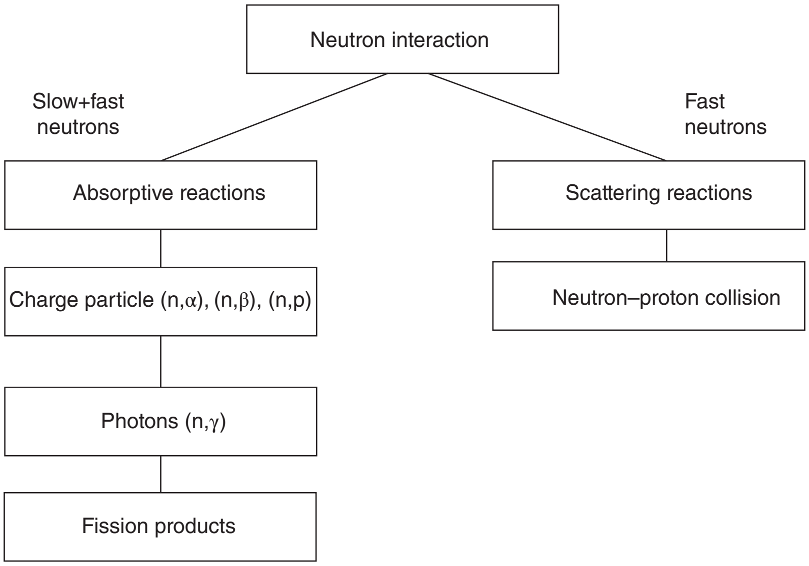

Figure 1.4.1 The classification of nuclear reactions between neutrons and nuclei.

Following Figure 1.4.1, all interaction events result in the emission of charged particles or γ photons, or fission fragments (heavy-charged particles), or a combination of them. This means that solid-state radiation detectors can be used indirectly, i.e. to map *the reaction products* in space and time as well as to measure their energy distributions. Processing all this information and solving relevant inverse problems restores the microscopic dynamics of reactions. The dynamics, in its turn, enables the derivation of characteristics parameters of the incoming neutron flux, such as its intensity, energy distribution, timing, etc.

Neutron absorbers can be fabricated out of various materials, such as filling gases, solid-state thin-film coatings, foils, etc. However, most often solid-state-sandwiched detectors incorporate stable isotopes with a high conversion efficiency of neutron energy into charge (or fission fragments, γ-rays). The stable isotopes of practical devices facilitate usually two absorbing nuclear reactions [19]. These are $^{10}B(n,\alpha)^7Li$ and $^6Li(n,\alpha)^3H$.

1.4.1 $^{10}B(n,\alpha)^7Li$ Nuclear Reaction

The interaction of a neutron with ^{10}B is shown schematically in Figure 1.4.2. On the neutron absorption, two charged particles are released in the opposite directions, i.e.

$$^{10}B + n \rightarrow \{^7Li(0.840\ \text{MeV}) + \alpha(1.470\ \text{MeV})\} \tag{1.4.3}$$

which accounts for approximately 93.7% of nuclear reactions with thermal neutrons ($E_k = 0.0259$ eV) or

$$^{10}B + n \rightarrow \{^7Li(1.015\ \text{MeV}) + \alpha(1.777\ \text{MeV})\} \tag{1.4.4}$$

generated in the remaining 6.3% of reactions. ^7Li(0.840 MeV) ions are born originally in the initial excited state. Very quickly (fractions of picoseconds), they relax to the stable ground state by emitting γ photons with an energy of 0.48 MeV.

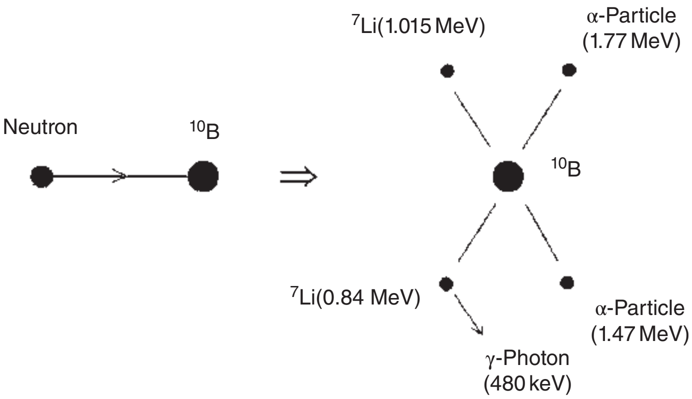

Figure 1.4.2 $^{10}B(n,\alpha)^7Li$ and $^{10}B(n,\gamma)^7Li$ nuclear reactions.

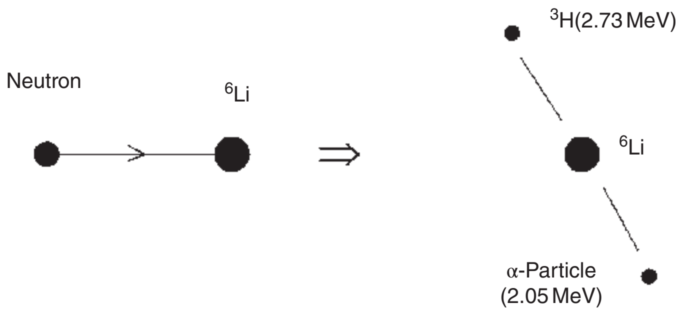

Figure 1.4.3 ^{6}Li(n, α)^{3}H nuclear reaction.

1.4.2 ^{6}Li(n,α)^{3}H Nuclear Reaction

This nuclear reaction is illustrated in Figure 1.4.3. On absorption of a neutron, two different charged particles are released in the opposite directions, i.e.

$$^6\text{Li} + {}^1_0\text{n} \rightarrow {}^3\text{H}(2.73\ \text{MeV}) + \alpha(2.05\ \text{MeV}) \tag{1.4.5}$$

This reaction is preferred when a detector of choice can demonstrate an extended efficiency in stopping longer-range α-particles due to their higher energy: 2.05 MeV, as opposite to 1.47 MeV in the ^{10}B reaction. In general, the intended application type governs decisions on the absorber material, detection method, sensor geometry, etc. Similar to sensors measuring other nuclear particles, the neutron detectors are also optimized for achieving the best possible detection efficiency, signal-to-background ratio, timing, and spatial resolution.

The attenuation function of the monoenergetic and monodirectional neutron flux in the detection media can be approximated by [4]

$$I = I_0 \mathrm{e}^{-\mu_{abs} x} \tag{1.4.6}$$

where I_0 is the intensity of the incoming beam, μ_{abs} is the attenuation coefficient given by the sum of the individual attenuation coefficients

$$\mu_{abs} = \mu_{capture} + \mu_{elastic} + \mu_{inelastic} = \frac{N_a \rho}{A} \sigma_{abs} \tag{1.4.7}$$

Here, σ_{abs} represents the cross sections of the absorber material as defined by Eq. (1.4.1). As we mentioned earlier in commenting Eq. (1.4.2), the absorption cross section is energy dependent. The energy dependence can be approximated by the following relationship [20]:

$$\sigma_{abs}(E) = \sigma_{abs}(E_0)\sqrt{\frac{E_0}{E}} \tag{1.4.8}$$

where $\sigma_{abs}(E_0)$ is a known absorbing cross section at some energy E_0.

On top of the monotonous functionality given by Eq. (1.4.8), the total cross section exhibits resonance peaks when energies of incoming neutrons come close to the energy levels available for occupation in the target nuclei.

In practice, the attenuation function may deviate significantly from the form defined by Eq. (1.4.6) due to various reasons. Some of them are listed as follows:

1) Incoming neutron fluxes are rarely monoenergetic. To accommodate the energy distribution, Eq. (1.4.7) should include the macroscopic cross sections averaged across the whole energy range of particles in the beam.
2) Elastic scatterings from nuclei do not remove particles from the beam, but just redistribute the neutron density $n_n(E_k)$, increasing the spectral density content at lower kinetic energies.
3) Neutrons can be scattered in directions other than the direction of the beam flow so that one has to deal with the total fluctuating neutron flux rather than the monodirectional constant neutron current.
4) The possible influence of edge effects, bearing in mind that the neutron beam cannot be focused to a very small diameter.

More precise expressions for the attenuation function can be found in specialized literature, for instance [5, 19].

The cross sections of ^{10}B(n,α)^{7}Li and ^{6}Li(n,α)^{3}H reactions are $3840\frac{\lambda}{1.8}$ barns and $940\frac{\lambda}{1.8}$ barns, respectively. Here, λ is the mean free path of the neutron or an average length between interactions.

The detection efficiency of absorbers is given by

$$\varepsilon = 1 - \exp(-N\sigma_{abs} t) \tag{1.4.9}$$

where N is the number density of the absorber and t is the thickness of the absorber. The product $\Sigma_{abs} = N\sigma_{abs}$ is usually referred to as the thermal-averaged macroscopic neutron absorption coefficient. It can be found in tabulated form, for instance, in [20].

An example of a double absorber neutron solid-state sensor is presented in Figure 1.4.4 [21–23]. The sensor incorporates two principal components as follows:

1) A neutron absorber that reacts to the incident neutron flux by generating charged particles (and γ-rays, for instance, in the $^{10}B(n,\alpha)^7Li$ reaction).
2) A secondary charged particle or γ-ray detector to measure products of nuclear reactions released by the neutron absorber.

The combined device is usually fabricated by *ex situ* coating the particle detector-sensitive volume with a layer containing either ^6Li or ^{10}B isotopes. Various coating techniques can be used, e.g. evaporation, sputtering, or chemical deposition. In some applications, a flip-chip configuration with *ex situ* prepared "foils" can be the preferred option. This approach works well with a wider range of neutron reactive materials – multilayer absorbers. It simplifies the processing steps and causes less damage to the secondary particle detectors.

The quantum efficiency of the coated neutron detector is quite low. There are several reasons for that:

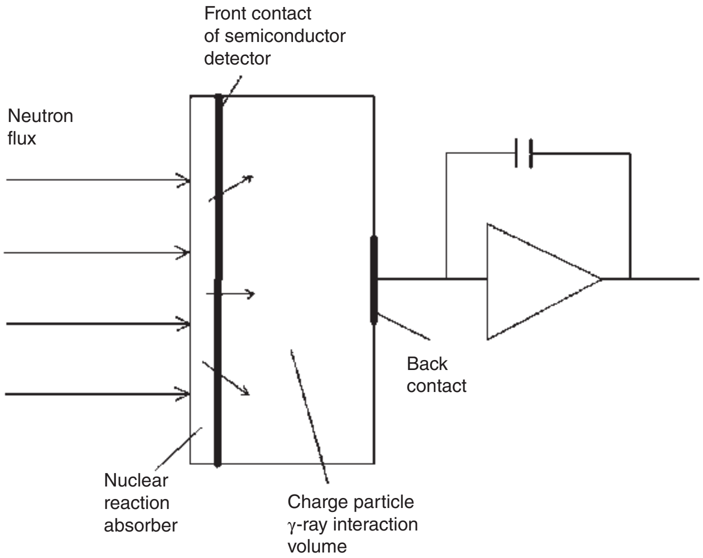

Figure 1.4.4 An example of the sandwiched neutron solid-state sensor incorporating two principal components: a neutron absorber that reacts to the incident neutron flux and γ-ray/charged particle detector to count and measure products of nuclear reactions coming out of the neutron absorber.

1) The double absorber detectors are only perceptive to the neutrons engaged in nuclear reactions within the thickness of the isotope enriched coat. The coat needs to be thinner than the range, R, of the lowest energy generated charged particle for it to be able to reach the secondary particle detector. For a thickness greater than R, the quantum efficiency drops rapidly as some reaction products relax in the coat itself partially or completely. This further complicates the restoration of neutron characteristics due to the reaction product charge collection deficit. The authors of [22] presented a comprehensive characterization of the pure ^{10}B film that enables the fast definition of the coating thickness during the fabrication steps. They measured an average effective ranges for a 0.84 MeV ^7Li, $L_{\mathrm{Li}(0.84\,\mathrm{MeV})} = 0.81\,\mu\mathrm{m}$, and a 1.47 MeV α-particle, $L_{\alpha(1.47\,\mathrm{MeV})} = 2.65\,\mu\mathrm{m}$, a microscopic thermal neutron absorption cross section $\sigma_{abs} = 3840\,\mathrm{b}$, and an atomic density 1.3×10^{23} atoms/cm^3. The average effective range here means an average distance over which a particle travels within the absorber until its energy decreases below the minimum detection threshold defined electronically by a low-level discriminator setting.

   The product of $\sigma_{abs}N$ yields a macroscopic absorption cross section $\Sigma_{abs} = 500\,\mathrm{cm}^{-1}$ and a measure of film stopping efficiency at $t = L$: $\Sigma_{abs}L_{\mathrm{Li}(0.84\,\mathrm{MeV})} = 0.0405$, $\Sigma_{abs}L_{\alpha(1.47\,\mathrm{MeV})} = 0.1324$.

   In the case of the ^6LiF coating, $\sigma_{abs} = 940\,\mathrm{b}$, $\Sigma_{abs} = 57.51\,\mathrm{cm}^{-1}$, $\Sigma_{abs}L_{3\mathrm{H}(2.73\,\mathrm{MeV})} = 0.1682$, $\Sigma_{abs}L_{\alpha(2.05\,\mathrm{MeV})} = 0.0267$. The figures were quoted for a minimum detection threshold of 300 keV. Interested readers can also find in McGregor et al. [22] tables for average effective ranges and reaction $\Sigma_{abs}L$ products calculated for detection thresholds from 100 to 800 keV.
2) It is reasonable to assume that nuclear reactions between neutrons and target nuclei release charged particles in all directions (4π sr full solid angle) with equal probability. The actual output signal is formed only by those nuclear reactions whose products travel within a solid angle that subtends the secondary particle detector absorber. For the detector configuration depicted in Figure 1.4.4, a solid angle is approximately 2π sr. In addition to that, the secondary sensor can detect only one product particle per reaction since the second one is emitted in an opposite direction.

The efficiency of solid-state neutron detectors can be doubled by constructing sandwiched configuration involving two secondary particle detectors on both sides of the neutron absorber. In this case, a solid angle approaches nearly 4π sr. However, the quantum efficiency limitation imposed by the film thickness is fundamental. It can be circumvented by stacking several individual devices in series [23].

Energies of nuclear reaction products between neutrons and target isotopes are large enough to be measured by conventional techniques, such as gas proportional counters, ionization chambers, and scintillation detectors. However, some specialized applications tend to engage the solid-state detectors where the compactness and low power consumption are at a premium. For instance, with this technology, the prospects of multipixel imaging arrays of solid-state detectors for neutron computed tomography (NCT) look very promising. Excellent performance of GaAs Schottky barrier detectors has been demonstrated when operating in the high energy radiation environment, which was the main limiting factor in the past, preventing their use in the NCT systems [23].

1.5 Heat Generation in Athermal Quasiparticle Absorbers

Energy deposited by incoming particle fluxes into a detection absorber divides between the electronic and phonon systems. A part of the phonon energy that does not create quasiparticles dissipates in the detector volume as heat. The heat needs to be quantified to make sure that all detector components operate at specified optimum temperatures. This is particularly important in the following cases:

a) For low-temperature sensors mounted on cold stages of refrigerators with limiting cooling capacity.
b) Detectors operating in a vacuum with weak thermal coupling to the radiators.
c) When there is a need to calculate the thermal link parameters/geometry for a detector exposed to high-intensity beams. Temperature elevation can be found using the following semiempirical equation:

$$\Delta T \approx \frac{4.8 E_p\, I_{beam}}{d_0 C_\Sigma (T_b)} \tag{1.5.1}$$

where E_p (keV) is the energy of the incident beam and C_Σ(W/cmK) is the combined thermal conductivity of the detector material and a thermal link from the detector to the heat sink. T_b is the base temperature of the heat sink, d_0 is the cross section of the radiation beam, and I_{beam} is the beam current. Equation (1.5.1) does not take into account other heat sources like the electric bias across the detector, heat generation by readout or conducting leads, etc. In semiconductor detectors operating under the reverse bias, electric particles relax down to kinetic energies defined by the net electric field rather than to the lattice temperature T_L, before they are removed from the interaction volume. This somewhat reduces the energy transfer to the lattice and ΔT.

References

1 J. Allison, K. Amako, J. Apostolakis, et al. Recent developments in GEAN4. *Nucl. Instrum. Methods Phys. Res., Sect. A* 835, 186 (2016).
2 N. Murray, A. Holland, D. Smith, et al. The X-ray quantum efficiency measurement of high resistivity CCDs. *Nucl. Instrum. Methods Phys. Res., Sect. A* 604, 180 (2009).
3 (2022) http://www.cxro.lbl.gov/optical_constants/atten2.html.
4 W. Leo. *Techniques for Nuclear and Particle Physics Experiments*. Springer-Verlag, 1994.
5 W. Tait. *Radiation Detection*. Butterworths, 1980.
6 K. Kanaya, S. Okayama. Penetration and energy-loss theory of electrons in solid targets. *J. Phys. D: Appl. Phys.* 5, 43 (1972).
7 P. Potts. *A Handbook of Silicate Rock Analysis*. Blackie, 1987.
8 J. Ashley. Energy-loss probabilities for electrons, positrons, and protons in condensed matter. *J. Appl. Phys.* 69, 674 (1991).
9 D. Penn. Electron mean-free-path calculations using a model dielectric function. *Phys. Rev. B* 35, 482 (1987).
10 J. Ashley, C. Tung, V. Anderson. Calculations of mean free paths and stopping powers of low energy electrons (<10 keV) in solids using a statistical model. *IEEE Trans. Nucl. Sci.* ND-23, 1833 (1976).
11 S. Tanuma, C. Powell, D. Penn. Calculations of electron inelastic mean free path for 31 materials. *Surf. Interface Anal.* 11, 577 (1988).
12 S. Tanuma, C. Powell, D. Penn. Calculations of electron inelastic mean free paths. II. Data for 27 elements over the 50–2000 eV range. *Surf. Interface Anal.* 17, 911 (1991).
13 H.A. Kramers. On the theory of X-ray absorption and of the continuous X-ray spectrum. *Phil. Mag.* 46, 836 (1923).
14 L. Yuan, C. Wu, Eds., *Methods of Experimental Physics: Nuclear Physics*, 5, 1 (1961).
15 W. Bragg, R. Kleeman. On the α particles of radium, and their loss of range in passing through various atoms and molecules. *London, Edinburgh, Dublin Phil. Mag. J. Sci.* 10, 318 (1905).

16 P. Ouseph. *Introduction to Nuclear Radiation Detectors*. Springer, 2012.

17 A. Compton. A quantum theory of the scattering of X-rays by light elements. *Phys. Rev.* 21, 483 (1923).

18 M. Cooper, P. Mijnarends, N. Shiotani, et al. *X-ray Compton Scattering*. Oxford Science Publications, 2005.

19 C. Grupen. *Particle Detectors*. Cambridge University Press, 1996.

20 J. Marion, J. Fowler, Eds., *Fast Neutron Physics, Part II: Experiment and Theory*. Wiley, NY, 1963.

21 D. McGregor, R. Klann, H. Gersch, et al. Designs for thin-film-coated semiconductor thermal neutron detectors. *IEEE Trans. Nucl. Sci.* 4, 2454–2458 (2001).

22 D. McGregor, M. Hamming, Y. Yang, et al. Design considerations for thin film coated semiconductor thermal neutron detectors – I: basics regarding alpha particle emitting neutron reactive films. *Nucl. Instrum. Methods Phys. Res., Sect. A* 500, 272 (2003).

23 R.G. Fronk, S.L. Bellinger, L.C. Henson, et al. High efficiency microstructured semiconductor neutron detectors for direct ^{3}He replacement. *Nucl. Instrum. Methods Phys. Res., Sect. A* 779, 25 (2015).